VNU Journal of Science: Mathematics – Physics, Vol. 39, No. 4 (2023) 14-25

VNU Journal of Science: Mathematics - Physics

Journal homepage: https://js.vnu.edu.vn/MaP

Original Article

Buckling and Post-buckling of Sandwich Plate with Functionally Graded Graphene Origami Reinforced Core Layer in Hygrothermal Environment

Vu Minh Anh*, Ngo Dinh Dat, Nguyen Dinh Duc

VNU University of Engineering and Technology, 144 Xuan Thuy, Cau Giay, Hanoi, Vietnam

Received 29 July 2023
Revised 11 August 2023; Accepted 14 August 2023

Abstract: The buckling and post-buckling of magneto-electric-elastic (MEE) sandwich plate are presented. The core layer consists of epoxy matrix reinforced with graphene origami auxetic metal-material in which the volume fraction of graphene origami is assumed to vary the thickness direction in three different distributions. For MEE face sheets, the proportions of ferroelectric and ferromagnetic components are chosen equally. The Reddy's higher order shear deformation plate theory forms the basis for establishing the governing equations. The axial compressive loading-deflection amplitude relation and the expression of critical buckling loading are obtained through the application of Galerkin method. The method's accuracy is validated by comparing its results with those published by other authors. The influences of various parameters on the buckling and post-buckling of the sandwich plate are investigated in details.

Keywords: Buckling and post-buckling; sandwich plate; graphene origami; auxetic metal-material; hygrothermal environment.

1. Introduction

Recently, there has been significant attention on novel three-dimensional structures called graphene origami and kirigami, owing to their remarkable mechanical, electronic, and optical properties. Jiang et al., [1] presented the design and bandgap optimization of multi-scale composite origami-inspired metamaterials reinforced with grapheme platelets and carbon fibers based on the Mindlin plate theory, higher-order spectral elements, and the Bloch theorem. Within the framework of the first-order shear

* Corresponding author.
E-mail address: vuminhanhhp@gmail.com

https//doi.org/10.25073/2588-1124/vnumap.4866

deformation beam theory, Zhao et al., [2] investigated the free vibration behavior and dynamic responses of functionally graded beams composed of novel graphene origami-enabled auxetic metal metamaterials subjected to an impulsive load. Based on the molecular dynamic simulations, Fan and Shen [3] designed a novel metamaterial which incorporates origami-graphene with single crystal copper matrix. Murari et al., [4] presented a numerical study on nonlinear free vibration and post-buckling behaviors of functionally graded graphene origami-enabled auxetic metamaterial tapered beams immersed in fluid, with a particular focus on the effect of negative Poisson's ratio on the nonlinear frequencies and post-buckling equilibrium paths. Using molecular dynamics simulations, Luo et al., [5] managed to effectively simulate the controlled graded release of C_{60} and C_{180} from a graphene box, drawing inspiration from the origami technique and employing an external electric field.

Due to their remarkable properties in both ferroelectricity and ferromagnetism, the MEE materials have emerged as a cutting-edge smart material of the next generation, capturing significant interest from scientists worldwide due to its wide-ranging applications across various industries. Esen and Ozmen [6] investigated the thermal vibration and buckling of magneto-electro-elastic functionally graded porous nanoplates using nonlocal strain gradient elasticity. Thai et al., [7] presented a nonlocal strain gradient iso-geometric model, which includes the higher-order shear deformation theory, nonlocal strain gradient theory and iso-geometric analysis method, for free vibration analysis of functionally graded nanoplates made of magneto-electro-elastic materials. Further, Zhou and Qu [8] introduced the magneto-electro-elastic coupling iso-geometric analysis method for the static and dynamic analysis of magneto-electro-elastic structures under thermal loading. In 2022, the nonlinear static buckling analysis of MEE sandwich plate on Pasternak-type elastic foundations subjected to the mechanical, thermal, electric and magnetic loadings is presented in the work of Quang et al., [9]. Jena et al., [10] presented an XFEM-based framework to model the semipermeable crack in magneto-electro-elastic material in which the interaction-integral technique is modified and implemented to extract the normalized magnetic induction intensity factor. Barati and Shariyat [11] proposed a novel analytical layer-dependent closed-form solution for multilayer magneto-piezo-elastic hollow spheres with anisotropic layers under asymmetric 2D magneto-electro-hygrothermo-mechanical loads.

This work introduces analytical approach for the buckling and post-buckling of the sandwich plate with functionally graded graphene origami reinforced core layer in hygrothermal environment. Three different distribution patterns of graphene are considered. The basic equations are derived by using the Reddy's higher order shear deformation plate theory and solved by using Galerkin method.

2. Problem Statement

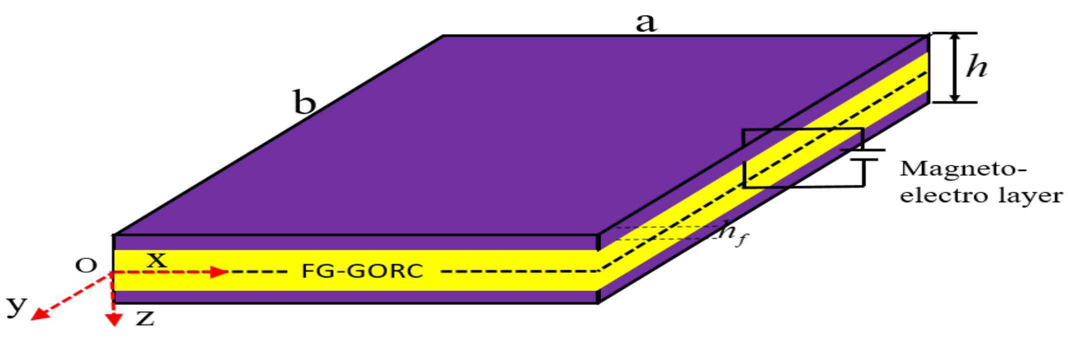

Figure 1. Modeling of the sandwich plate on Pasternak's type elastic foundations.

Let's take into consideration a smart sandwich plate with dimensions: length a, width b, and thickness h. This plate is composed of two magneto-electro-elastic face sheets and an epoxy matrix reinforced with a graphene origami core layer. The core layer, comprising NL layers, has a uniform thickness, resulting in a total thickness of h_c. Each face sheet has a thickness of h_f. To establish a coordinate system, we define xyz, where the xy plane represents the middle surface of the sandwich plate, and the z-axis corresponds to the thickness direction. Figure 1 shows a visual representation of the sandwich plate's geometrical parameters and coordinate system.

The volume faction of graphene origami corresponding to the three distribution patterns is expressed as follows [3, 4].

$$V_{Gr}(z)=\begin{cases} V_{Gr}^{*}\ (UD) \\ 2V_{Gr}^{*}\left(1-\left|2k-NL-1\right|/NL\right)\ (FG-O),\ V_{cu}(z)=1-V_{Gr}(z), \\ 2V_{Gr}^{*}\left(\left|2k-NL-1\right|/NL\right)\ (FG-X) \end{cases} \tag{1}$$

The Young's modulus, thermal expansion coefficient and Poisson's ratio of epoxy matrix reinforced with graphene origami auxetic metalmaterial core layer are [3, 4]

$$\begin{aligned} &E_c=\frac{1+\xi\eta V_{Gr}}{1-\eta V_{Gr}}E_{Cu}\times f_E\left(H_{Gr},V_{Gr},T\right), \\ &\alpha_c=\left(\alpha_{Gr}V_{Gr}+\alpha_{Cu}V_{Cu}\right)\times f_a\left(H_{Gr},V_{Gr},T\right), \\ &v_c=\left(v_{Gr}V_{Gr}+v_{Cu}V_{Cu}\right)\times f_v\left(H_{Gr},V_{Gr},T\right), \end{aligned} \tag{2}$$

with

$$\begin{aligned} &f_E\left(H_{Gr},V_{Gr},T\right)=1.11-1.22V_{Gr}-0.134\left(T/T_0\right)+0.559V_{Gr}\left(T/T_0\right)-5.5H_{Gr}V_{Gr} \\ &+38H_{Gr}V_{Gr}^2-20.6H_{Gr}^2V_{Gr}^2 \\ &f_\alpha\left(H_{Gr},V_{Gr},T\right)=0.794-16.8V_{Gr}^2-0.0279\left(T/T_0\right)^2+0.182\left(1+V_{Gr}\right)\left(T/T_0\right) \\ &f_v\left(H_{Gr},V_{Gr},T\right)=1.01-1.43V_{Gr}+0.165\left(T/T_0\right) \\ &-16.8H_{Gr}V_{Gr}-1.1H_{Gr}V_{Gr}\left(T/T_0\right)-16H_{Gr}^2V_{Gr}^2 f_\rho\left(V_{Gr},T\right)=1.01-2.01V_{Gr}^2-0.0131\left(T/T_0\right) \end{aligned} \tag{3}$$

The material properties of magneto-electro-elastic face sheets are given in Table 1 [9].

Table 1. Mechanical properties of magneto-electro-elastic face sheets

Material properties	Notation	Values
Elastic constants (GPa)	$C_{11}^f=C_{22}^f$	220
	$C_{12}^f=C_{13}^f=C_{23}^f$	120
Piezoelectric constants $\left(C/m^2\right)$	e_{31}	–3.5
	e_{33}	9.0
	e_{15}	0
Dielectric constants $\left(C/\mathrm{N}m^2\right)$	$\eta_{11}=\eta_{22}$	0.85×10^{-9}
	η_{33}	6.3×10^{-9}
Magnetic permeability $\left(\mathrm{Ns}^2/\mathrm{C}^2\right)$	$\mu_{11}=\mu_{22}$	-2×10^{-4}
	μ_{33}	0.9×10^{-4}

3. Governing Equations

The force and moment resultants of the sandwich plate are defined as

$$\left(N_i, M_i, P_i\right)=\int_{-\frac{h_c}{2}-h_f}^{-\frac{h_c}{2}} \sigma_i^f\left(1, z, z^3\right)dz+\sum_{j=1}^{NL}\int_{-\frac{h_c}{2}+(j-1)\frac{h_c}{NL}}^{-\frac{h_c}{2}+j\frac{h_c}{NL}} \sigma_i^C\left(1, z, z^3\right)dz+\int_{\frac{h_c}{2}}^{\frac{h_c}{2}+h_f} \sigma_i^f\left(1, z, z^3\right)dz,$$
$$\left(Q_i, R_i\right)=\int_{-\frac{h_c}{2}-h_f}^{-\frac{h_c}{2}} \sigma_{iz}^f(1, z^2)dz+\sum_{j=1}^{NL}\int_{-\frac{h_c}{2}+(j-1)\frac{h_c}{NL}}^{-\frac{h_c}{2}+j\frac{h_c}{NL}} \sigma_{iz}^C(1, z^2)dz+\int_{\frac{h_c}{2}}^{\frac{h_c}{2}+h_f} \sigma_{iz}^f(1, z^2)dz, \quad (4)$$

The geometrical compatibility equation for the sandwich plate is written as

$$\begin{aligned}&I_{21}\left(\frac{\partial^4}{\partial x^4}\wp(x,y)\right)+I_{11}\left(\frac{\partial^4}{\partial y^4}\wp(x,y)\right)+M_1\left(\frac{\partial^4}{\partial y^2\partial x^2}\wp(x,y)\right)+M_2\frac{\partial^3\phi_x}{\partial x^3}+\\&M_3\frac{\partial^3\phi_x}{\partial x\partial y^2}+M_4\frac{\partial^3\phi_y}{\partial y^3}+M_5\frac{\partial^3\phi_y}{\partial y\partial x^2}-c_1I_{25}\frac{\partial^4 w}{\partial x^4}-c_1I_{16}\frac{\partial^4 w}{\partial y^4}+M_6\frac{\partial^4 w}{\partial x^2\partial y^2}\\&-\left(\left(\frac{\partial^2 w}{\partial x\partial y}\right)^2-\frac{\partial^2 w}{\partial x^2}\frac{\partial^2 w}{\partial y^2}+2\frac{\partial^2 w}{\partial x\partial y}\frac{\partial^2 w^*}{\partial x\partial y}-\frac{\partial^2 w}{\partial x^2}\frac{\partial^2 w^*}{\partial y^2}-\frac{\partial^2 w}{\partial y^2}\frac{\partial^2 w^*}{\partial x^2}\right)=0,\end{aligned} \quad (5)$$

where

$$\begin{aligned}&M_1=I_{31}-2I_{12},\ M_2=I_{23}-c_1I_{25},\ M_3=I_{13}-c_1I_{15}-I_{32}+c_1I_{33},\\&M_4=I_{14}-c_1I_{16}, M_5=I_{24}-c_1I_{26}-I_{32}+c_1I_{33},\ M_6=-c_1I_{15}-c_1I_{26}+2c_1I_{33}.\end{aligned} \quad (6)$$

The equilibrium equation of the sandwich plate is expressed as follows

$$\begin{aligned}&L_{11}(w)+L_{12}(\phi_x)+L_{13}(\phi_y)+L_{14}(f)++L_{15}(\Phi)+L_{16}(\Psi)+S(w,f)+S^*(w^*,f)=0,\\&L_{21}(w)+L_{22}(\phi_x)+L_{23}(\phi_y)+L_{24}(f)+L_{21}^*(w^*)+L_{25}(\Phi)+L_{26}(\Psi)=0,\\&L_{31}(w)+L_{32}(\phi_x)+L_{33}(\phi_y)+L_{34}(f)+L_{31}^*(w^*)+L_{35}(\Phi)+L_{36}(\Psi)=0,\\&\int_{-h_c/2-h_f}^{h_c/2}\left(\frac{\partial D_x}{\partial x}\cos(\beta z)+\frac{\partial D_y}{\partial y}\cos(\beta z)+D_z\beta\sin(\beta z)\right)dz\\&+\int_{h_c/2}^{h_c/2+h_f}\left(\frac{\partial D_x}{\partial x}\cos(\beta z)+\frac{\partial D_y}{\partial y}\cos(\beta z)+D_z\beta\sin(\beta z)\right)dz=0,\\&\int_{-h_c/2-h_f}^{h_c/2}\left(\frac{\partial B_x}{\partial x}\cos(\beta z)+\frac{\partial B_y}{\partial y}\cos(\beta z)+B_z\beta\sin(\beta z)\right)dz\\&+\int_{h_c/2}^{h_c/2+h_f}\left(\frac{\partial B_x}{\partial x}\cos(\beta z)+\frac{\partial B_y}{\partial y}\cos(\beta z)+B_z\beta\sin(\beta z)\right)dz=0,\end{aligned} \quad (7)$$

in which the parameters $L_{1i}, L_{2i}, L_{3i}\ (i=\overline{1,6}), S$ are expressed in Appendix A.

The strain compatibility equation is defined as

$$I_{21}\left(\frac{\partial^4}{\partial x^4}\wp(x,y)\right)+I_{11}\left(\frac{\partial^4}{\partial y^4}\wp(x,y)\right)+J_1\left(\frac{\partial^4}{\partial y^2\partial x^2}\wp(x,y)\right)+J_2\frac{\partial^3\phi_x}{\partial x^3}+$$
$$J_3\frac{\partial^3\phi_x}{\partial x\partial y^2}+J_4\frac{\partial^3\phi_y}{\partial y^3}+J_5\frac{\partial^3\phi_y}{\partial y\partial x^2}-c_1I_{25}\frac{\partial^4 w}{\partial x^4}-c_1I_{16}\frac{\partial^4 w}{\partial y^4}+J_6\frac{\partial^4 w}{\partial x^2\partial y^2} \tag{8}$$
$$-\left(\frac{\partial^2 w}{\partial x\partial y}^2-\frac{\partial^2 w}{\partial x^2}\frac{\partial^2 w}{\partial y^2}+2\frac{\partial^2 w}{\partial x\partial y}\frac{\partial^2 w^*}{\partial x\partial y}-\frac{\partial^2 w}{\partial x^2}\frac{\partial^2 w^*}{\partial y^2}-\frac{\partial^2 w}{\partial y^2}\frac{\partial^2 w^*}{\partial x^2}\right)=0,$$

in which

$$J_1=I_{31}-2I_{12},\ J_2=I_{23}-c_1I_{25},\ J_3=I_{13}-c_1I_{15}-I_{32}+c_1I_{33},$$
$$J_4=I_{14}-c_1I_{16}, J_5=I_{24}-c_1I_{26}-I_{32}+c_1I_{33},\ J_6=-c_1I_{15}-c_1I_{26}+2c_1I_{33}. \tag{9}$$

The boundary conditions assume that the four edges of the imperfect sandwich plate are simply supported as

$$w=N_{xy}=M_x=0, N_x=N_x^0\ \ at\ \ x=0,\ a,$$
$$w=N_{xy}=M_y=0,\ N_y=N_y^0\ \ at\ \ y=0,\ b. \tag{10}$$

The problem's solutions consist of a double trigonometric function that meets the given boundary condition as follows

$$\{w(x,y,t),\Phi(x,y,t),\Psi(x,y,t)\}=\{W(t),\phi(t),\psi(t)\}\sin\lambda_m x\sin\delta_n y,$$
$$\phi_x(x,y,t)=\Phi_x(t)\cos\lambda_m x\sin\delta_n y,\phi_y(x,y,t)=\Phi_y(t)\sin\lambda_m x\cos\delta_n y, \tag{11}$$
$$w^*(x,y,t)=\mu h\sin\lambda_m x\sin\delta_n y$$
$$f(x,y,t)=P_1(t)\cos 2\lambda_m x+P_2(t)\cos 2\delta_n y+P_3(t)\sin\lambda_m x\sin\delta_n y+\frac{1}{2}N_{y0}x^2+\frac{1}{2}N_{x0}y^2$$

where

$$P_1=\frac{\delta_n^2}{32I_{21}\lambda_m^2}W(W+2\mu h),P_2=\frac{\lambda_m^2}{32I_{11}\delta_n^2}W(W+2\mu h),\ P_3=Q_1W+Q_2\Phi_x+Q_3\Phi_y. \tag{12}$$

with $\lambda=m\pi/a,\ \beta=n\pi/b.$

Applying the Bubnov - Galerkin method to Eq. (7) after replacing Eq. (11) results in

$$p_{11}W+p_{12}\Phi_x+p_{13}\Phi_y+p_{14}(\mathrm{W}+\mu h)\Phi_x+p_{15}(\mathrm{W}+\mu h)\Phi_y+p_{16}\phi+p_{17}\psi$$
$$+\left[n_1-N_{x0}\lambda_m^2-N_{y0}\delta_n^2\right](W+\mu h)+n_2W(W+\mu h) \tag{13}$$
$$+n_3W(W+2\mu h)+n_4W(W+\mu h)(W+2\mu h)=0,$$
$$p_{21}\mathrm{W}+p_{22}\Phi_x+p_{23}\Phi_y+p_{24}\phi+p_{25}\psi+n_6(W+\mu h)+n_7W(W+2\mu h)=0,$$
$$p_{31}\mathrm{W}+p_{32}\Phi_x+p_{33}\Phi_y+p_{34}\phi+p_{35}\psi+n_8(W+\mu h)+n_9W(W+2\mu h)=0,$$
$$p_{41}\mathrm{W}+p_{42}\Phi_x+p_{43}\Phi_y+p_{44}\phi+p_{45}\psi=0$$
$$p_{51}\mathrm{W}+p_{52}\Phi_x+p_{53}\Phi_y+p_{54}\phi+p_{55}\psi=0$$

where the coefficients p_{ij} may be found in Appendix B.

The reaction forces on two sides $y=0,b$ is determined as

$$N_{y0} = -F_x h \frac{I_{12}}{I_{21}} + f_1 W + f_4 \left(W + 2\mu h \right) W + f_2 \Phi_x + f_3 \Phi_y + f_5 \Phi_1 + f_6 \Phi_2 \tag{14}$$

where

$$\begin{gathered} f_1 = -\frac{a_4}{abI_{21}} \frac{4}{\lambda_m \delta_n}, \; f_4 = \frac{1}{8} \frac{\left(\delta_n^{\;2}\right)}{I_{21}}, \; f_2 = -\frac{\left(a_5\right)}{ab\left(I_{21}\right)} \frac{4}{\lambda_m \delta_n}, \\ f_3 = -\frac{\left(a_6\right)}{ab\left(I_{21}\right)} \frac{4}{\lambda_m \delta_n}, \; f_5 = -\frac{\left(I_{27}\right)}{\left(I_{21}\right)}, \; f_6 = -\frac{\left(I_{28}\right)}{\left(I_{21}\right)}, \; f_7 = -\frac{\left(I_{29}\right)}{\left(I_{21}\right)}, \; f_8 = -\frac{\left(I_{30}\right)}{\left(I_{21}\right)} \\ a_4 = \left(-Q_1 I_{21} \lambda_m^{\;2} + \delta_n^{\;2} Q_1 I_{12} + c_1 I_{26} \delta_n^2 + c_1 I_{25} \lambda_m^2 \right), a_5 = \left(\left(-I_{23} + c_1 I_{25} \right) \lambda_m + I_{12} Q_2 \delta_n^{\;2} - I_{21} Q_2 \lambda_m^{\;2} \right) \\ a_6 = \left(\left(-I_{24} + c_1 I_{26} \right) \delta_n + I_{12} Q_3 \delta_n^{\;2} - I_{21} Q_3 \lambda_m^{\;2} \right) \end{gathered} \tag{15}$$

Introducing Eq. (14) into Eqs. (13), we have the axial compressive load - deflection relation as

$$F_x = b_{11}^s \frac{\overline{W}}{\left(\overline{W} + \mu\right)} + b_{12}^s + b_{13}^s \overline{W} + b_{14}^s \frac{\overline{W}\left(\overline{W} + 2\mu\right)}{\left(\overline{W} + \mu\right)} + b_{15}^s \left(\overline{W} + \mu\right) + b_{16}^s \overline{W}\left(\overline{W} + 2\mu\right) \tag{16}$$

where

$$\begin{gathered} b_{11}^s = -\frac{b_{11}}{h\left(\lambda_m^2 + \frac{I_{12}}{I_{21}} \delta_n^2\right)}, b_{12}^s = -b_{12} \frac{1}{h\left(\lambda_m^2 + \frac{I_{12}}{I_{21}} \delta_n^2\right)}, b_{13}^s = -\frac{b_{13}}{\left(\lambda_m^2 + \frac{I_{12}}{I_{21}} \delta_n^2\right)} \\ b_{14}^s = -\frac{b_{14}}{\left(\lambda_m^2 + \frac{I_{12}}{I_{21}} \delta_n^2\right)}, b_{15}^s = -\frac{b_{15}}{\left(\lambda_m^2 + \frac{I_{12}}{I_{21}} \delta_n^2\right)}, b_{16}^s = -\frac{b_{16} h}{\left(\lambda_m^2 + \frac{I_{12}}{I_{21}} \delta_n^2\right)} \end{gathered} \tag{17}$$

The critical buckling load is obtained as:

$$F_{xcr} = b_{11}^s + b_{12}^s \tag{18}$$

4. Results and Discussion

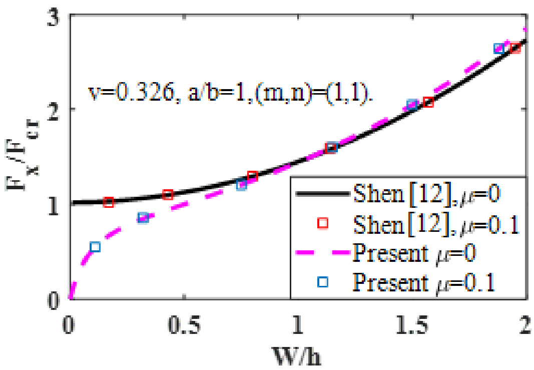

Figure 2. Comparison of the load–deflection curves of compressive isotropic plate.

In order to validate the method and showcase the findings, a comparison between the load-deflection curves of a compressive isotropic plate and Shen's numerical results was made [12], employing Reddy's higher order shear deformation theory. Figure 2 illustrates a remarkable resemblance between the outcomes presented in the study and Shen's results. This similarity serves to affirm the reliability of the method utilized.

Table 2 presents a comprehensive analysis of the critical buckling load of a sandwich plate in a thermal environment, focusing on the influence of three key factors: the weight fraction of graphene origami, magnetic potential, and the plate width to thickness ratio. The investigation encompasses three distinct weight fraction levels of graphene origami, three magnetic potential levels, and four plate width to thickness ratios.

Table 2. Effects of the weight fraction of graphene origami, magnetic potential, and the width to thickness ratio on the critical buckling loading of the sandwich plate

W_{Gr}		b/h			
	$\psi_0\,(A)$	10	15	20	25
1.5	-200	3.8293	1.7056	0.9285	0.5625
2		5.1205	2.2885	1.2558	0.7699
2.5		12.1147	5.4651	3.0436	1.9036
1.5	0	3.8300	1.7067	0.9300	0.5643
2		5.1215	2.2900	1.2578	0.7724
2.5		12.1166	5.4680	3.0436	1.9036
1.5	200	3.8308	1.7078	0.9314	0.5661
2		5.1224	2.2915	1.2597	0.7749
2.5		12.1185	5.4709	3.0475	1.9084

To begin with, it is observed that the weight fraction of graphene origami significantly impacts the stiffness of the sandwich plate, consequently leading to a noteworthy increase in the critical buckling load. As the weight fraction of graphene origami rises, the sandwich plate's stiffness experiences an appreciable enhancement, resulting in an augmented critical buckling load. On the other hand, the effect of magnetic potential on the critical buckling load appears to be relatively subtle. Although there is a slight increase in the critical buckling load with the increment of magnetic potential, its influence remains comparably minor compared to other factors.

From Table 3, one can observe the effects of various factors, namely, the degrees of graphene origami folding, total number of layers, and temperature increment, on the critical buckling load (GPa) of the sandwich plate. Notably, as the temperature increment rises, the critical buckling load experiences a significant decrease. This outcome is unsurprising as temperature has a detrimental impact on both the elastic modulus and stiffness of the sandwich plate, leading to reduced load-bearing capacity. Moreover, the critical buckling load displays substantial growth with increasing graphene origami folding degrees or total number of layers. This enhancement can be attributed to the corresponding increase of the structural stiffness of the sandwich plate. The greater the graphene origami folding degrees or the total number of layers, the higher the resistance to buckling, thus resulting in a notable boost in the critical buckling load.

Table 3. Effects of the graphene origami folding degrees, total number of layers and temperature change on the critical buckling loading of the sandwich plate

H_{Gr}	NL	ΔT		
		0	50	100
60%	6	1.2506	1.1868	1.1220
80%		1.3065	1.2389	1.1707
100%		1.3447	1.2729	1.2010
60%	8	1.2645	1.2030	1.1404
80%		1.3275	1.2620	1.1958
100%		1.3787	1.3082	1.2376
60%	10	1.2712	1.2112	1.1501
80%		1.3380	1.2738	1.2089
100%		1.3971	1.3277	1.2578

Figures 3 and 4 display the impact of the weight fraction and the distribution pattern of graphene origami on the axial compressive loading – dimensionless deflection curves of the sandwich plate on elastic foundations in a thermal environment. The results indicate that the load carrying capacity of the sandwich plate increases with higher weight fractions of graphene. This improvement can be attributed to the reinforcement effect of graphene, which enhances the structural stiffness of the sandwich plate, leading to a higher load carrying capacity. Furthermore, the distribution pattern of graphene also plays a significant role in determining the load carrying capacity. The sandwich plate with a UD distribution pattern of graphene exhibits the lowest load carrying capacity, while FG-O follows with slightly better performance. Notably, the sandwich plate with FG-X demonstrates the highest load carrying capacity among the three patterns studied. This disparity can be attributed to the varying distribution of graphene within the texture of the sandwich plate, influencing its overall mechanical properties. Specifically, higher graphene is concentrated on the middle plane of sandwich plate with the FG-O distribution pattern while the large concentration of graphene on the top and bottom faces with FG-X distribution pattern.

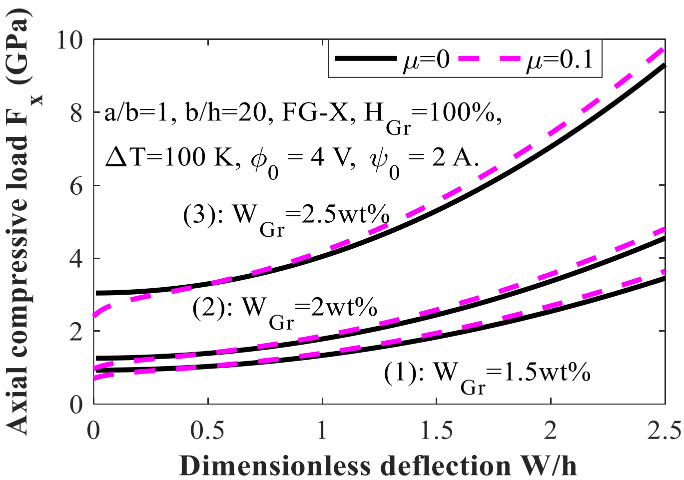

Figure 3. Effect of volume fraction of graphene on the axial compressive loading – dimensionless deflection curves of the sandwich plate.

Figure 5 shows the impact of different degrees of graphene origami folding on the dimensionless deflection curves of a sandwich plate under axial compressive loading, combined with thermal, electric, and magnetic loadings. Three values of graphene origami folding degrees ($H_{GR} = 60\%, 80\%, 100\%$) are considered. It is evident that as the graphene origami folding degrees increase, the load-carrying capacity of the sandwich plate also increases. This phenomenon is attributed to the development of auxetic behavior in the sandwich plate as the graphene origami folding degrees rise.

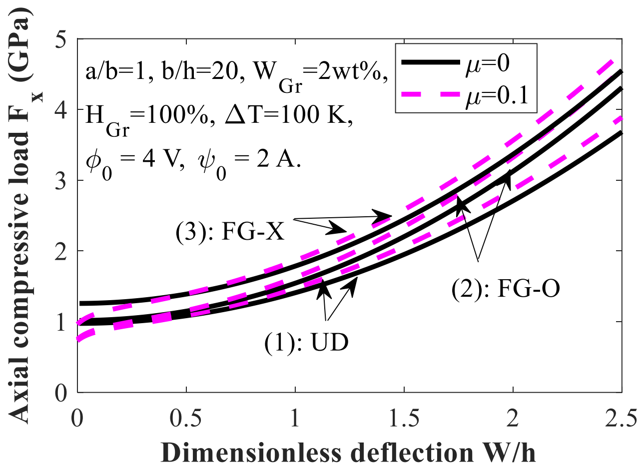

Figure 4. Effect of distribution pattern of graphene on the axial compressive loading – dimensionless deflection curves of the sandwich plate.

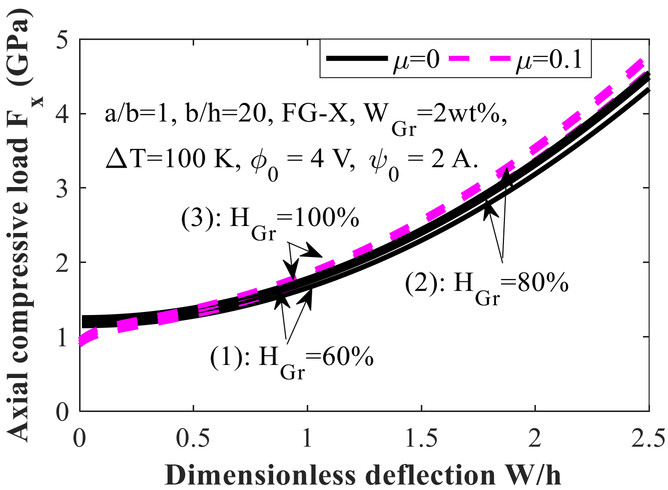

Figure 5. Effect of graphene origami folding degrees on the axial compressive loading – dimensionless deflection curves of the sandwich plate.

Figure 6 displays the influence of the total number of layers on the axial compressive loading – dimensionless deflection curves of the sandwich plate on elastic foundations in a thermal environment. The data clearly indicates a gradual enhancement in the load-carrying capacity of the sandwich plate with an increasing total number of layers. This phenomenon can be explained by the concurrent rise in the structural stiffness of the sandwich plate, which is directly proportional to the augmentation of layers.

As the total number of layers grows, the sandwich plate exhibits improved resistance to compressive loads, resulting in a higher load-carrying capability. This behavior is a result of the added structural integrity and mechanical strength imparted by each additional layer, leading to an overall incremental enhancement in load-bearing performance.

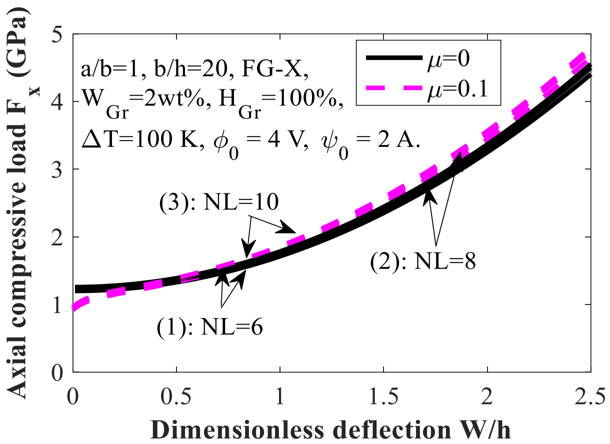

Figure 6. Effect of total number of layers on the axial compressive loading – dimensionless deflection curves of the sandwich plate.

5. Conclusions

In this work we focused on the investigation of the nonlinear buckling and post-buckling behaviors of an imperfect magneto-elastic-electric sandwich plate. The Galerkin method is employed to determine crucial findings such as the critical buckling load and the load carrying capacity of the sandwich plate. From the obtained numerical results, following notable conclusions can be drawn:

- An increase in the weight fraction of graphene origami leads to a simultaneous increase in both the critical buckling loading and the load carrying capacity of the sandwich plate.

- With a rise in the total number of layers, the critical buckling load and load carrying capacity show a slight increase.

- Different distribution patterns of graphene exhibit distinct load carrying capacities. The sandwich plate with a UD distribution pattern of graphene exhibits the lowest load carrying capacity, followed by FG-O with slightly better performance.

- The critical buckling loading of the sandwich plate experiences a significant reduction as the temperature increment is increased. This highlights the vulnerability of the plate to buckling under higher temperatures.

- The geometric parameters have a substantial impact on the nonlinear buckling and post-buckling behavior of the sandwich plate.

Acknowledgments

This research is funded by the Project number CN.22.11 of VNU Hanoi – University of Engineering and Technology. The authors are grateful for this support.

References

[1] J. T. Q. Han, C. Li, Design and Bandgap Optimization of Multi-Scale Composite Origami-Inspired Metamaterials, International Jounal of Mechanical Sciences, Vol. 248, 2023, pp. 108233, https://doi.org/10.1016/j.ijmecsci.2023.108233.

[2] S. Zhao, Y. Zhang, J. Yang, S. Kitipornchai, Vibrational Characteristics of Functionally Graded Graphene Origami-Enabled Auxetic Metamaterial Beams Based on Machine Learning Assisted Models, Aerospace Science and Technology, Vol. 130, 2022, pp. 107906, https://doi.org/10.1016/j.ast.2022.107906.

[3] Y. Fan, H. S. Shen, Non-Symmetric Stiffness of Origami-Graphene Metamaterial Plates, Compososite Structure, Vol. 297, 2022, pp. 115974, https://doi.org/10.1016/j.compstruct.2022.115974.

[4] B. Murari, S. Zhao, Y. Zhang, J. Yang, Graphene Origami-Enabled Auxetic Metamaterial Tapered Beams in Fluid: Nonlinear Vibration and Postbuckling Analyses Via Physics-Embedded Machine Learning Model, Applied Mathematical Modelling, Vol. 122, 2023, pp. 598-613, https://doi.org/10.1016/j.apm.2023.06.023.

[5] S. Luo, A. S. Ademiloye, Z. Wu, Y. Zhang, Molecular Hierarchical Release using Hydrogenated Graphene Origami Under Electric Field, Materials Science in Semiconductor Processing, Vol. 131, 2021, pp. 105844, https://doi.org/10.1016/j.mssp.2021.105844.

[6] I. Esen, R. Özmen, Thermal Vibration and Buckling of Magneto-Electro-Elastic Functionally Graded Porous Nanoplates using Nonlocal Strain Gradient Elasticity, Composite Structure, Vol. 296, 2022, pp. 115878, https://doi.org/10.1016/j.compstruct.2022.115878.

[7] C. H. Thai, A. M. J. Fereira, N. X. Hung, P. T. Hung, P. V. Phung, A Nonlocal Strain Gradient Isogeometric Model for Free Vibration Analysis of Magneto-Electro-Elastic Functionally Graded Nanoplates, Composite Structure, Vol. 316, 2023, pp. 117005, https://doi.org/10.1016/j.compstruct.2023.117005.

[8] L. Zhou, F. Qu, The Magneto-Electro-Elastic Coupling Isogeometric Analysis Method for the Static and Dynamic Analysis of Magneto-Electro-Elastic Structures Under Thermal Loading, Composite Structure, Vol. 315, 2023, pp. 116984, https://doi.org/10.1016/j.compstruct.2023.116984.

[9] V. D. Quang, T. Q. Quan, P. Chan, Static Buckling Analysis and Geometrical Optimization of Magneto-Electro-Elastic Sandwich Plate with Auxetic Honeycomb Core, Thin-Walled Structures, Vol. 173, 2022, pp. 108935, https://doi.org/10.1016/j.tws.2022.108935.

[10] J. Jena, I. V. Singh, V. Gaur, A Numerical Study of Semipermeable Cracks in Magneto-Electro-Elastic Material Using XFEM, Engineering Fracture Mechanics, Vol. 275, 2022, pp. 108817, https://doi.org/10.1016/j.engfracmech.2022.108817.

[11] A. R. Barati, M. Shariyat, Novel Exact Layerwise Analytical Solution for Anisotropic Multi-Layer Magneto-Piezo-Elastic Hollow Spheres Under Asymmetric Magneto-Electro-Hygro-Thermo-Mechanical Loads, Composite Structure, Vol. 302, 2022, pp. 116227, https://doi.org/10.1016/j.compstruct.2022.116227.

[12] H. S. Shen, Postbuckling of FGM Plates with Piezoelectric Actuators Under Thermo-Electro-Mechanical Loadings, International Journal of Solids and Structure, Vol. 42, 2005, pp. 6101-21, https://doi.org/10.1016/j.ijsolstr.2005.03.042.

Appendixes

Appendix A

$$L_{11}\left(w\right)=O_{11}\frac{\partial^2 w}{\partial x^2}+O_{12}\frac{\partial^2 w}{\partial y^2}+O_{13}\frac{\partial^4 w}{\partial x^4}+O_{14}\frac{\partial^4 w}{\partial x^2\partial y^2}+O_{15}\frac{\partial^4 w}{\partial y^4}-k_1 w+k_2\left(\frac{\partial^2 w}{\partial x^2}+\frac{\partial^2 w}{\partial y^2}\right),$$

$$L_{12}\left(\phi_x\right)=O_{11}\frac{\partial \phi_x}{\partial x}+O_{16}\frac{\partial^3 \phi_x}{\partial x^3}+O_{17}\frac{\partial^3 \phi_x}{\partial x\partial y^2},\ L_{13}\left(\phi_y\right)=O_{12}\frac{\partial \phi_y}{\partial y}+O_{18}\frac{\partial^3 \phi_y}{\partial y^3}+O_{19}\frac{\partial^3 \phi_y}{\partial x^2\partial y},$$

$$L_{14}(f)=O_{110}\frac{\partial^4 f}{\partial x^4}-X_{110}\eta\left(\frac{\partial^6}{\partial x^6}\wp\left(x,y\right)+\frac{\partial^6}{\partial y^2\partial x^4}\wp\left(x,y\right)\right)+O_{111}\frac{\partial^4 f}{\partial x^2\partial y^2}$$

$$-O_{111}\eta\left(\frac{\partial^6}{\partial x^2\partial y^4}\wp(x,y)+\frac{\partial^6}{\partial y^2\partial x^4}\wp(x,y)\right)+O_{112}\frac{\partial^4 f}{\partial y^4}-$$

$$O_{112}\eta\left(\frac{\partial^6}{\partial y^6}\wp(x,y)+\frac{\partial^6}{\partial x^2\partial y^4}\wp(x,y)\right),L_{15}(\Phi)=\left(O_{114}\cos(\beta z)-O_{115}\beta\sin(\beta z)\right)\frac{\partial^2\Phi}{\partial^2 x}$$

$$+\left(O_{113}\cos(\beta z)-O_{116}\beta\sin(\beta z)\right)\frac{\partial^2\Phi}{\partial^2 y},L_{21}(w)=O_{21}\frac{\partial w}{\partial x}+O_{22}\frac{\partial^3 w}{\partial x^3}+O_{23}\frac{\partial^3 w}{\partial x\partial y^2},$$

$$L_{22}(\phi_x)=O_{21}\phi_x+O_{24}\frac{\partial^2\phi_x}{\partial x^2}+O_{25}\frac{\partial^2\phi_x}{\partial y^2},L_{23}(\phi_y)=O_{26}\frac{\partial^2\phi_y}{\partial x\partial y},\ L_{24}(f)=O_{27}\frac{\partial^3 f}{\partial x^3}\left(1-\eta\left(\frac{\partial^2 f}{\partial x^2}+\frac{\partial^2 f}{\partial y^2}\right)\right)$$

$$+O_{28}\frac{\partial^3 f}{\partial x\partial y^2}\left(1-\eta\left(\frac{\partial^2 f}{\partial x^2}+\frac{\partial^2 f}{\partial y^2}\right)\right),L_{25}(\Phi)=-\left(O_{114}\cos(\beta z)+O_{29}\beta\sin(\beta z)\right)\frac{\partial\Phi}{\partial x}$$

$$L_{26}(\Psi)=-\left(O_{118}\cos(\beta z)+O_{210}\beta\sin(\beta z)\right)\frac{\partial\Psi}{\partial x},L_{31}(w)=O_{31}\frac{\partial w}{\partial y}+O_{32}\frac{\partial^3 w}{\partial x^2\partial y}+O_{33}\frac{\partial^3 w}{\partial y^3},$$

$$L_{32}(\phi_x)=O_{34}\frac{\partial^2\phi_x}{\partial x\partial y},L_{33}(\phi_y)=O_{31}\phi_y+O_{35}\frac{\partial^2\phi_y}{\partial x^2}+O_{36}\frac{\partial^2\phi_y}{\partial y^2},\ L_{34}(f)=O_{37}\frac{\partial^3 f}{\partial x^2\partial y}\left(1-\eta\left(\frac{\partial^2 f}{\partial x^2}+\frac{\partial^2 f}{\partial y^2}\right)\right)$$

Appendix B

$$p_{11}=\left(l_{11}+l_{16}h_{11}+l_{17}h_{21}\right),p_{12}=\left(l_{12}+l_{16}h_{12}+l_{17}h_{22}\right),p_{13}=\left(l_{13}+l_{16}h_{13}+l_{17}h_{23}\right),$$
$$p_{21}=\left(l_{21}+l_{24}h_{11}+l_{25}h_{21}\right),p_{22}=\left(l_{22}+l_{24}h_{12}+l_{25}h_{22}\right),p_{23}=\left(l_{23}+l_{24}h_{13}+l_{25}h_{23}\right),$$
$$p_{31}=\left(l_{31}+l_{34}h_{11}+l_{35}h_{21}\right),p_{32}=\left(l_{32}+l_{34}h_{12}+l_{35}h_{22}\right),p_{33}=\left(l_{33}+l_{34}h_{13}+l_{35}h_{23}\right),$$